catalysts

MDPI

Article

Nano-Magnetic Sugarcane Bagasse Cellulosic Composite as a Sustainable Photocatalyst for Textile Industrial Effluent Remediation

Maha A. Tony [1,*], Nour Sh. El-Gendy [2,3], Mohamed Hussien [4], Abdullah A. S. Ahmed [5], Jiayu Xin [6,7], Xingmei Lu [6,7,8] and Ibrahim El Tantawy El-Sayed [5,*]

1 Advanced Materials/Solar Energy and Environmental Sustainability (AMSEES) Laboratory, Basic Engineering Science Department, Faculty of Engineering, Menoufia University, Shebin El-Kom, Menoufia 32511, Egypt
2 Egyptian Petroleum Research Institute (EPRI), Nasr City, Cairo 11727, Egypt; nourepri@yahoo.com or nshelgendy@msa.edu.eg
3 Center of Excellence, October University for Modern Sciences and Arts (MSA), 6th of October City, Giza 12566, Egypt
4 Department of Chemistry, Faculty of Science, King Khalid University, 9004, Aseer, Abha 61413, Saudi Arabia; mhalmosylhy@kku.edu.sa
5 Department of Chemistry, Faculty of Science, Menoufia University, Shebin El-Kom, Menoufia 32511, Egypt; abdullahahmed@science.menofia.edu.eg
6 Beijing Key Laboratory of Ionic Liquids Clean Process, CAS Key Laboratory of Green Process and Engineering, State Key Laboratory of Multiphase Complex Systems, Innovation Academy for Green Manufacture, Institute of Process Engineering, Chinese Academy of Sciences, Beijing 100190, China; jyxin@ipe.ac.cn (J.X.); xmlu@ipe.ac.cn (X.L.)
7 Sino Danish College, University of Chinese Academy of Sciences, Beijing 100049, China
8 School of Chemistry and Chemical Engineering, University of Chinese Academy of Sciences, Beijing 100049, China
* Correspondence: maha.shalaby@sh-eng.menofia.edu.eg (M.A.T.); ibrahimtantawy@science.menofia.edu.eg (I.E.T.E.-S.)

check for updates

Citation: Tony, M.A.; El-Gendy, N.S.; Hussien, M.; Ahmed, A.A.S.; Xin, J.; Lu, X.; El-Sayed, I.E.T. Nano-Magnetic Sugarcane Bagasse Cellulosic Composite as a Sustainable Photocatalyst for Textile Industrial Effluent Remediation. *Catalysts* **2024**, *14*, 354. https://doi.org/10.3390/catal14060354

Academic Editors: Didier Robert and Bo Weng

Received: 30 March 2024
Revised: 20 May 2024
Accepted: 24 May 2024
Published: 30 May 2024

Abstract: Researchers have focused on deriving environmentally benign materials from biomass waste and converting them into value-added materials. In this study, cellulosic crystals derived from sugarcane bagasse (SCB) are augmented with magnetite (M) nanoparticles. Following the co-precipitation route, the composite was prepared, and then the mixture was subjected to a green microwave solvent-less technique. Various mass ratios of SCB:M (1:1, 2:1, 3:1, 5:1, and 1:2) were prepared and efficiently utilized as photocatalysts. To look at the structural and morphological properties of the prepared samples, X-ray diffraction pattern (XRD), scanning electron microscopy (SEM), and elemental analysis were used to describe the composite fibers. SCB:M augmented with H_2O_2 as a Fenton reaction was used to eliminate Reactive blue 19 (RB19) from polluted water and was compared with pristine SCB and M. Additionally, the response surface methodology (RSM) statistically located and assessed the optimized parameters. The optimal operating conditions were recorded at pH 2.0 and 3:1 SCB: M with 40 mg/L and 100 mg/L of hydrogen peroxide. However, the temperature increase inhibits the oxidation reaction. The kinetic modeling fit showed the reaction following the second-order kinetic model with an energy barrier of 98.66 kJ/mol. The results show that such photocatalyst behavior is a promising candidate for treating textile effluent in practical applications.

Keywords: sugarcane bagasse cellulose; ionic liquid; textile effluent; photocatalysis; magnetite; reactive blue 19; kinetics

1. Introduction

Forestry generates massive wastes comprising lignocellulosic residues, including sawdust, bark, sugarcane bagasse, and other wood waste [1,2]. Sugarcane bagasse (SCB),

commonly named bagasse, is an agro-waste that mainly contains holo-cellulose (61.2%), lignin (25.6%), extractive (9.3%), and ash (3.9%) [1,3]. Sugarcane bagasse development and applications for numerous utilizations are gaining much attention as a sustainable material. However, the challenge of transforming them from underrated waste into economically viable beneficial material still persists [1]. Of these applications, using sugarcane bagasse for wastewater (WW) treatment is attaining the scientists' interest.

Due to technological advances, the demand for water for industrial uses is increasing. Consequently, industrial organic matter contaminates water, leading to a significant global environmental problem [4]. Therefore, significant health hazards are caused when such wastewater is released into the ecosystem, and it needs treatment before final disposal for a green environment [5]. Upon the comparison of existing wastewater treatment methodologies, advanced oxidation processes (AOPs) are signified as an efficient tool for wastewater remediation since they are simple and cost-efficient techniques for eliminating various types of pollutants from aqueous effluents, under the researchers' best role scenario, achieving 'cradle-to-cradle' (CRD) status as a cleaner, low-cost, and superior solution furnished to fight environmental destruction. In this regard, the modified Fenton reaction, which combines iron with H_2O_2, is introduced and has a vital role as one of the AOPs [6]. Until now, most studies cited in the literature have primarily relied on using iron salts to lead to Fenton's reaction.

Overall, sugarcane bagasse, in its unmodified and original form, is suitable for wastewater treatment owing to its properties [1]. Generally, sugarcane bagasse has been applied to eliminate numerous types of pollutants from aqueous streams, i.e., dyes [7], heavy metals [8], oil [9], and arsenic compounds [10]. However, the use of sugarcane bagasse incorporated with iron nanoparticles as a photocatalyst is limited in the literature for dye removal. Searching for various scenarios to attain a reliable Fenton's system reaction is gaining researchers' attention. To gain a better reaction, it is essential to frontier Fenton research. To overcome the disadvantages of the homogenous Fenton system, a heterogeneous catalyst is introduced [6]. In this regard, the research conducted for supporting iron material as a heterogeneous carrier is essential; for example, previous research applied zeolite as a Fenton-support material [11,12]. Also, other work shows oxalic acid/iron catalyst combinations to prevent iron settling [13].

It is worth recalling that using eco-friendly solvents, ionic liquids (ILs) are a privilege and an effective tool in the pretreatment of various biomass materials. The distinct properties of ILs, such as low melting point, high thermal stability, and inexpensive cost, make them the most promising choice in different industrial applications [11]. Furthermore, the structural designability of these organic salts and their versatility allow them to be synthesized and utilized for their intended applications. The variation in ionic liquids on organic cations and organic and inorganic anions forms acidic, basic, neutral, and amphoteric ionic liquids, depending on the type of the presented cations or anions [12].

Cholinium-based ionic liquids are promising eco-friendly solvents due to their biodegradability and inexpensive cost. Choline belongs to quaternary ammonium salts incorporated with counter-anions such as chloride or hydroxide utilized as precursors and cation sources for the formation of different ionic liquids for various applications [12–14].

Cholinium-amino acid ionic liquids [Ch][AA] find utility in various applications due to their low toxicity, biocompatibility, and biodegradability. The eco-friendly preference of cholinium-amino acid compared to other ionic liquids containing phosphorus, fluoro, and sulfur makes [Ch][AA] the best choice for different environmental applications [13,15].

Creating new materials from renewable stock resources that may be recycled renewed, or reused through natural processes is one way to design for a circular economy approach [14]. Rather than being thrown away, such product waste might be kept as a resource equivalent to the raw ingredients. The necessity of a circular economy is to increase awareness among procurers and consumers of the vital role that a given product plays, not just the product itself. Thus, a significant worldwide philosophical strategy encourages the recycling of short-lived products or by-product wastes for repeated use as beneficial

supplies. In addition to being recycled and reused to reduce the demand for the planet's limited resources, sugarcane bagasse is also regarded as a cradle-to-cradle (CRD) method for minimizing wastewater [15–18]. As a result, waste management takes precedence over it when considering the end-of-life alternative. Promoting the environmentally friendly use of renewable resources like wood and wood-based products is the main goal of the global bioeconomy strategy [19–21]. The objective is to utilize reuse, recycling, and renewal cycles to transform trash or industrial waste/by-products into new, value bio-based products in a sustainable way.

This work explores the extraction of valuable fibers from sugarcane bagasse through chemical treatment, aligning with environmental sustainability approaches and CRD waste management trends. Magnetite nanoparticles are prepared via the facile co-precipitation route, and the extracted sugarcane bagasse fiber is augmented with magnetite in different proportions through the microwave technique. XRD, SEM, and EDX analyses assessed the prepared materials. The novelty of such a study is introducing the sugarcane bagasse/magnetite composite as a photocatalyst to substitute the classical iron source to be mineralized via H_2O_2 for Reactive blue 19 oxidation. This, in turn, converts waste substances from discharge into a value-added product, minimizing environmental impact.

2. Results and Discussion

2.1. Cellulose Extraction from Sugarcane Bagasse Using Pretreatment Method

The extraction of cellulose from sugarcane bagasse was successfully achieved via the pretreatment of sugarcane bagasse with prepared cholinium-glycinate ionic liquid [Ch]Gly], starting with the addition of 25 g of [Ch][Gly] to 1.25 g of sugarcane bagasse followed by heating at 130 °C for 3 h. After the pretreatment process was accomplished, the mixture was poured into acetone/ethanol (1:1 v/v) to achieve cellulose with good yield.

2.2. Structural and Morphological Characterization

A cost-effective and benign strategy was used to synthesize the SCB-imbedded magnetite particles, as illustrated in Figure 1. XRD analysis was used to determine the crystalline behavior of the prepared SCB:M composite, which is displayed in Figure 1. The XRD pattern shows distinct peaks of pristine SCB (Figure 1a), magnetite (Figure 1b), and their composite at different ratios of metal and SCB (Figure 1c–g). The graphs highlight the intensive peaks and their changes in the composite (highlighted blue bars, Figure 1). As shown in Figure 1, two distinct peaks were detected in the pristine SCB at diffraction angles (2θ) of 15.6° and 22.4°, which confirm the presence of lattice plans (101) and (002) of cellulose I. Moreover, a tiny extra peak was noted at 2θ of 34.7°, corresponding to the (400) phase of the crystalline cellulose I [1]. Furthermore, the attained peaks corresponding to the investigated substance sample exposed the ferrite substance's single face-cantered cubic (FCC) spinel structure. The most intensive peaks (311), (440), and (220) correspond to 2θ of 35.52°, 62.84°, and 30.2°, respectively [13,14]. Moreover, the presence of other crystal plans (111), (422), (511), and (533) corresponds to 17°, 54.5°, 66.7°, and 74.8°, respectively, according to our previous published work [22], attributed to the presence of magnetite and exploring the successful creation of Fe_3O_4. Similar peaks were attained for the various examined SCB:M samples (Figure 1c–g), implying the successful augmentation of Fe_3O_4 with SCB, which confirms the presence of the magnetite peaks in SCB.

For the purpose of exploring the particle size distribution and surface morphology of the pristinely treated SCB and the composite nanoparticles, SEM images were taken (Figure 2). The size of the pristine SCB (Figure 2a) was hundreds of microns, and it controlled the structure of layers with variously arranged vessels between the layers. Such vessels and layers provide a significant amount of space for RB19 to react in polluted water. Figure 2b displays the magnetite nanoparticle SEM image that illustrates the existence of aggregated homogeneous sphere-shaped particles with a narrow grain size distribution as signified by the red circles in the micrograph (Figure 2b). The particle-size distribution of the attained material is located between the 20 and 60 nm ranges. Before augmentation

with magnetite, the surface of the SCB (Figure 2a) was smooth, and there were several folds between each vessel. However, Fe_3O_4 aggregates in a random distribution on the SCB surface after the magnetic modification, as illustrated in Figure 2c–g. For SCB augmented with Fe_3O_4 NPs in Figure 2c, the gloss change in the surface was due to the coverage of Fe_3O_4 for the SCB surface. That confirms the well- and uniformly covered SCB surface with Fe_3O_4 nanoparticles. The SEM analysis illustrates that the percentage of SCB added changes the intrinsic structure of SCB:M due to the increased or decreased mass/weight ratio of M and SCB, indicating the successful mixing of magnetite.

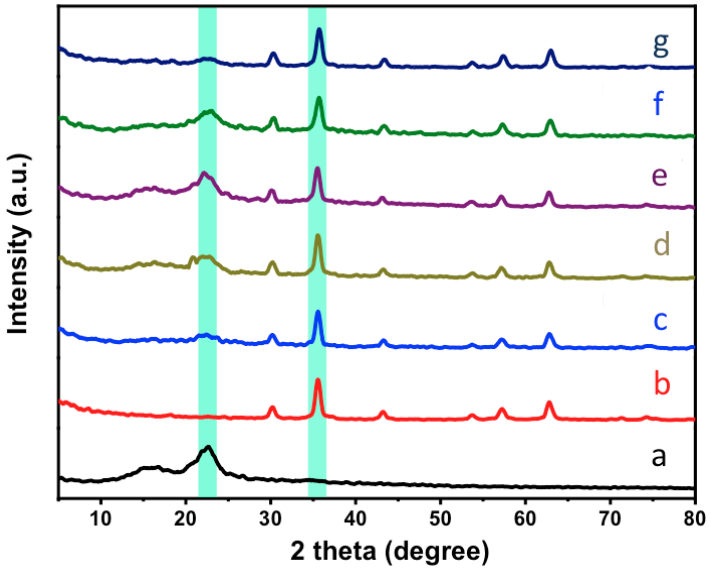

Figure 1. X-ray diffraction of different photocatalysts: (**a**) SCB:M (1:0); (**b**) SCB:M (0:1); (**c**) SCB:M (1:1); (**d**) SCB:M (2:1); (**e**) SCB:M (3:1); (**f**) SCB:M (5:1); and (**g**) SCB:M (1:2).

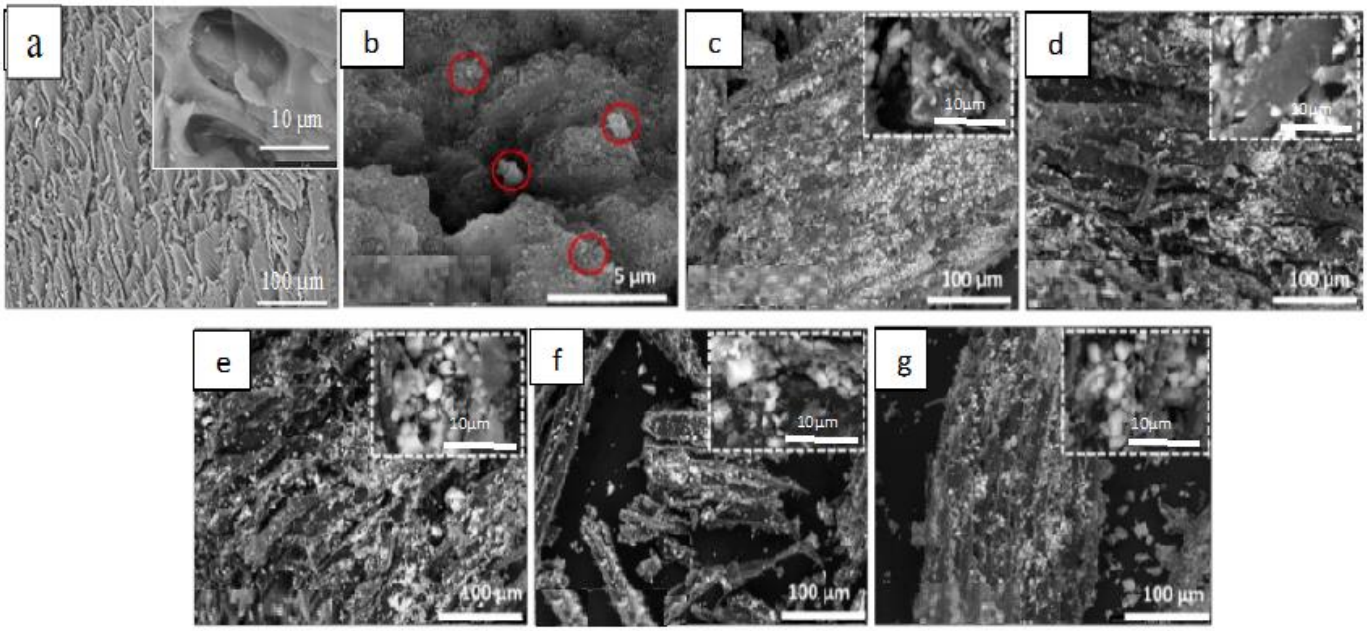

Figure 2. SEM images of (**a**) pristine SCB, (**b**) Fe_3O_4, (**c**) SCB:M (1:1), (**d**) SCB:M (2:1), (**e**) SCB:M (3:1), (**f**) SCB:M (5:1), and (**g**) SCB:M (1:2).

The EDX results of pristine SCB and SCB augmented with Fe_3O_4 NP (SCB:M 3:1) composite are displayed in Figure 3. The surface of solo SCB principally consisted of C (53.61%), Si (0.64%), and O (45.75%), while SCB augmented with Fe_3O_4 NPs mainly comprised C (22.63%), O (46.54%), Si (0.51%), and Fe (30.22%). The C percent presented a decline after adjustment and modifications, from 53.61% to 22.63%, due to SCB mainly consisting of C and O. In the spectrum of SCB augmented with Fe_3O_4 NPs, the peaks of Fe appeared, indicating the successful mixing of Fe_3O_4 and SCB. The two-dimensional EDX mappings of SCB and SCB mixed with Fe_3O_4 are given in Figure 3a,b, respectively. The C, O, Si, and Fe mappings accessible in SCB: M sample verify the uniform atom distribution, well equivalent with the SEM image.

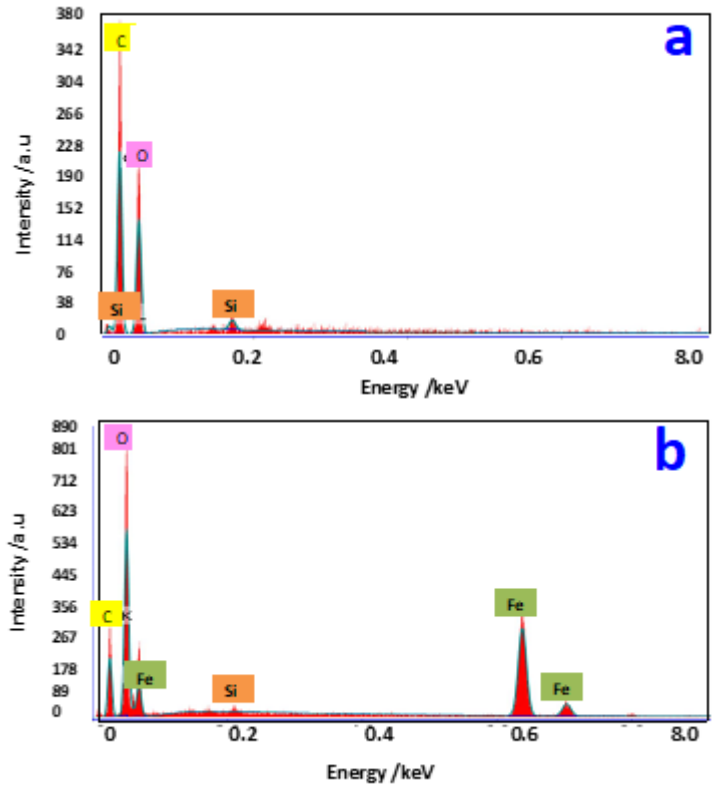

Figure 3. EDX spectra of (**a**) pristine SCB and (**b**) Fe_3O_4 nanoparticle-augmented SCB composite.

2.3. Optical and Magnetic Properties

The optical characteristic is vital for the photocatalytic material to catch light for additional oxidation reactions. In this regard, the obtained optical band gap of the SCB/magnetite (SCB:M 3:1) nanocomposite was signified by UV-Vis diffuse reflectance spectroscopy (UV–Vis DRS), and the spectrum is displayed in Figure 4a. According to the literature cited [17], the pristine Fe_3O_4 particles exhibit strong absorption in UV and visible light regions, as verified by their small band gap. Hence, after loading Fe_3O_4 on SCB cellulosic material, the spectrum reveals the absorption bands mainly in the ultraviolet region (200–400 nm) and less absorbance in the visible region. This indicates that the existence of Fe_3O_4 loading can enhance the photo-response range of the prepared composite.

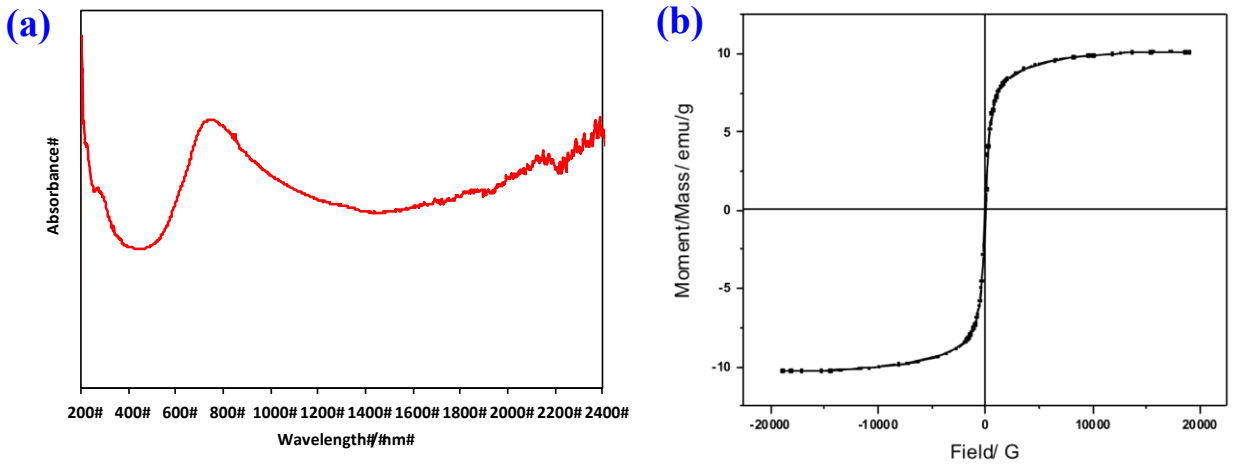

Figure 4. Optical and magnetic properties of the SCB/magnetite composite photocatalyst (SCB:M (3:1)). (**a**) UV-Vis and (**b**) VSM.

Vibrating sample magnetometer (VSM) analysis for the prepared substance investigated the behavior of magnetism for the SCB combined with Fe_3O_4 nanoparticles. Figure 4b illustrates the magnetization loop of the SCB/magnetite (SCB:M 3:1) nanoparticles at ambient temperature. The magnetic hysteresis data display the magnetic behavior. The substance showed a small amount of dissipated energy according to the plot of the hysteresis curve, which is signified as a narrow curve. VSM results indicate that the field required to magnetize the substance coercively (Hci) is 22.41 C. Also, retentivity (Mr), which corresponds to the field needed to degauss the substance, is 0.39525 emu/g. The value of the maximum magnetic moment per unit volume of the magnetized SCB substances is expressed as 10.213 emu/g, which verifies the appropriate magnetic behavior. The small coercive force approves the small area of the hysteresis loop and resembles residual magnetization at zero. Hence, it is estimated that the magnetic SCB materials loaded with pollutants could be easily removable and collected via an external magnetic field.

2.4. Photocatalytic Activity Comparison and Reaction Time Performances

A preliminary experiment for solo dye oxidation was conducted, and the data showed almost no oxidation without catalyst addition. The influences of reaction time on RB19 oxidation using SCB, magnetite (M), and sugarcane bagasse (SCB)/magnetite (M) catalytic materials under UV transmittance and without UV irradiance for Fenton's reaction were established to evaluate an experimental test condition for extra work. The comparative data in Figure 5a reveal the RB19 oxidation as a function of oxidation time via the various treatment reactions (a pH value of 3.0 using 40 and 400 mg/L concentrations of catalyst material and H_2O_2 doses, respectively). Such doses were selected as guidance for pre-examination. According to the experimental data, in the dark test, all the systems without ultraviolet illumination are not efficient in dye removal. Solo SCB, magnetite NPs, and SCB:M composite showed only 15, 6, and 23% dye removal, respectively. That might be related to adsorption removal. But, both SCB:M and magnetite catalyst-based Fenton reactions were efficient in RB19 removal from a polluted aqueous stream under UV illumination. The dye removal was enhanced and reached approximately 46 and 47%, respectively, within 5 min of oxidation. That confirms the photo-Fenton reaction. Nevertheless, only 37% of the RB19 was mineralized within 5 min of the UV-irradiance reaction time for the SCB-based treatment. However, with time, the dye oxidation was decelerated and the removal efficacy was alleviated in all of the studied cases. Thus, the interpretation of the obtained data would confirm that the dye removal would be due to an augmented oxidation/adsorption process. Such a high rate of mineralization at the preliminary oxidation time is associated with the $^{\cdot}OH$ radicals' generation, which could be steadily diminished with time. Moreover, the decrease in the H_2O_2 reagent dose with the existence of extra radical species that

hinders the removal rate rather than elevating the rate of reaction also declines the reaction. Generally, in the Fenton oxidation technique, the reaction occurs by exploiting the initiation of H_2O_2 with a catalyst for OH radical species production. However, the H_2O_2 is depleted by the end of the initial reaction period. A complex reaction generates hydroperoxyl radicals (HO_2). Hydroxyl and hydroperoxyl radicals both have an effect on the reaction, but hydroperoxyl radicals are less able to oxidize than hydroxyl radicals. Therefore, the dye's oxidation capacity declines with time. Numerous investigators recorded the rapid reaction rate at the initial reaction period as a consequence of the rapid formation of the OH species. Also, it is noteworthy to mention that the pristine magnetite catalyst is competitive with the Fe_3O_4 NP-augmented SCB composite. Thus, the utilization of waste SCB in the preparation of photocatalysts reduces the consumption of expensive magnetite NPs. Moreover, it minimizes the solid waste management problem and converts an unused waste material into a value-added recyclable photocatalyst, enriching the green economy.

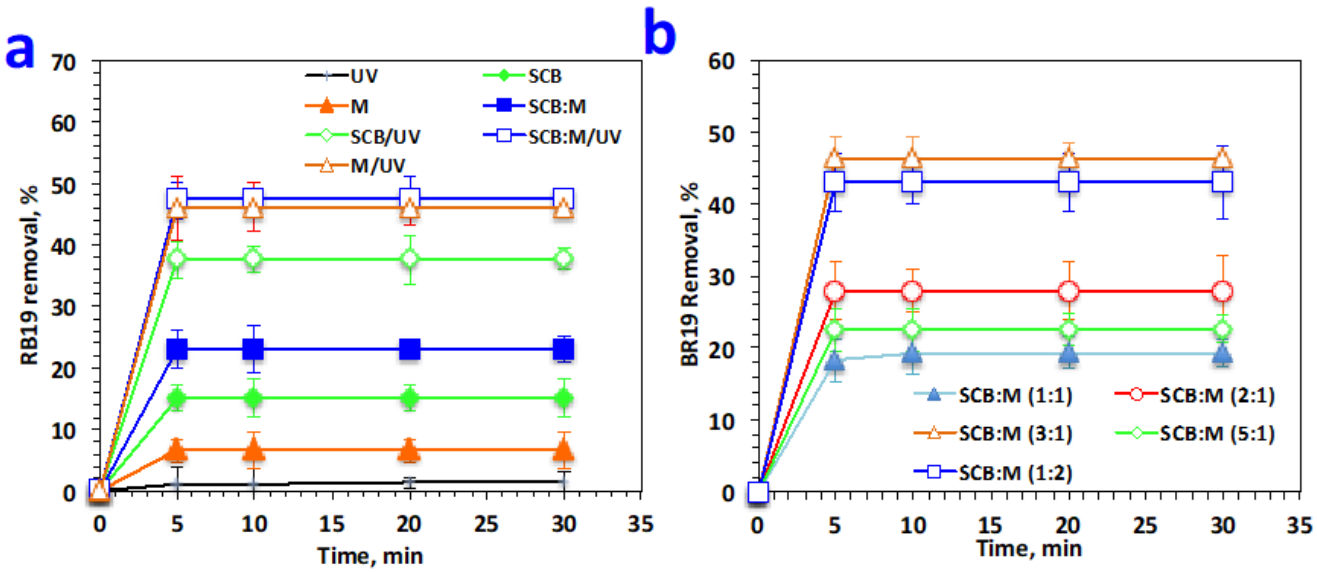

Figure 5. Oxidation tendency of Reactive blue 19 removals at (**a**) different oxidation systems; (**b**) various SCB:M mass ratios.

Although a similar trend of rapid oxidation occurs in the initial reaction time when a solo SCB catalyst is applied, the dye oxidation is associated with the coagulation reaction that only occurs with this technique. Such coagulation efficacy is correlated with its tendency to form multi-charged facilities for accumulating sorption uptake [7].

Following treatment and preparation, the microwave system adopts different mass proportions, SCB:M (1:1, 2:1, 3:1, 4:1, and 1:2), for the proper mixing of SCB and magnetite. Figure 5 displays the oxidation tendency of the various system-based Fenton reactions. The data confirmed the existence of both oxidation and adsorption processes. The percentage efficiency in all of the studied batches can be categorized as follows: 3:1 > 1:2 > 2:1 > 5:1 > 1:1 SCB:M (Figure 5b). Also, it is noteworthy to mention the almost-near results for the batches of SCB:M (3:1) and (1:2). This could be attributed to the oxidation/adsorption reaction, which could be associated with higher SCB levels, implying more adsorption, and an excess of M, indicating that the oxidation reaction contributes to dye removal during the adoption test. The results showed that the decreasing hydrophilicity of the SCB surface was caused by combining magnetite nanomolecules with a large SCB mass [18]. Accordingly, the combination of a 3:1 mass ratio was selected as the optimal SCB:M mass ratio composition for further testing.

2.5. Effect of Dye Loading

The preliminary Reactive blue 19 dye concentration in aqueous effluent influence on the RB19 removal efficacy by sorption/oxidation is exhibited in Figure 6 for the different systems, namely, SCB/H_2O_2/UV, M/H_2O_2/UV, and SCB:M/H_2O_2/UV systems. The preliminary H_2O_2 dosing was monitored at 400 mg/L and the magnetized SCB material dose of 40 mg/L at a pH value of 3.0, and the RB19 concentration ranged from 5 to 30 ppm. At a glance at Figure 6 for all systems, the highest RB19 oxidation efficacy was extended to a whole removal after 5 min, corresponding to the dye concentration of 5 ppm. However, an increase in the RB19 concentration resulted in a decrease in the mineralization efficacy.

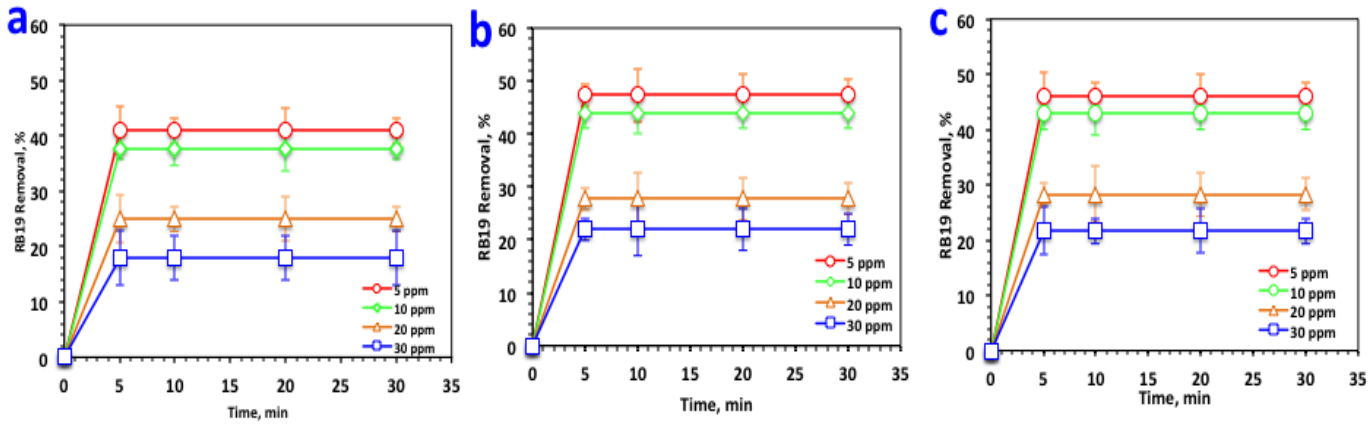

Figure 6. Effect of dye loading on the photocatalytic activity of (**a**) SCB; (**b**) M; (**c**) SCB:M systems.

So far, the reduction in the oxidation rate with the elevation in the RB19 dye dose could be explained by the fact that the amount of catalyst (SCB, M, or SCB:M) and H_2O_2 are constant in all the designs. Therefore, the quantity of H_2O_2 and catalyst amounts that are the chief producers of hydroxyl radicals, •OH, is not adequate for yielding sufficient OH species. Furthermore, the quantity of functional unoccupied adsorbent material, SCB, sites is too low for the extra RB19 loads in the polluted water effluent. Also, more dye loads on the catalyst, even at SCB or Fe_3O_4 active sites, consequently diminish the active •OH quantity. Previous investigators [19] recorded a parallel tendency for oxidizing and adsorbing azo dye and reactive dyes, respectively. Furthermore, at a very low dye concentration of 5 ppm, inhibition in the oxidation rate is observed for all the systems. This could be attributed to the low driving force [20].

2.6. Multiple Operating Parameters Effect

Catalyst, hydrogen peroxide, and pH influence: H_2O_2 decomposition in the presence of an SCB:M is crucial for the oxidation system to generate the highly oxidizing species, ·OH. But it is essential to minimize the H_2O_2 or catalyst concentrations, since their presence in greater dosages reduces the oxidation reaction yield. Hence, to explore the effect of various SCB:M on the oxidation of RB19, tests were carried out to examine the impact of catalyst material concentration on oxidation kinetics.

Figure 7a exhibits the influences of the elevation in the H_2O_2 reagent on the Reactive blue 19 oxidation reaction rate. However, all other variables persisted at constant values (catalyst material 40 mg/L and pH 3.0). The data reveal an enhancement in RB19 oxidation efficiency of 64% with the reduction in the peroxide dose to 100 mg/L, following previous exploration by Tzani et al. [13] in treating vehicle washing wastewater. Exceeding H_2O_2 dosage over the optimum needed dose, H_2O_2 performs as ·OH radical inhibitor instead of a generator. Therefore, a terminus dye oxidation reached only 32% with the excess H_2O_2 of 800 mg/L. Such investigation was stated previously by Rezgui and his co-workers [6].

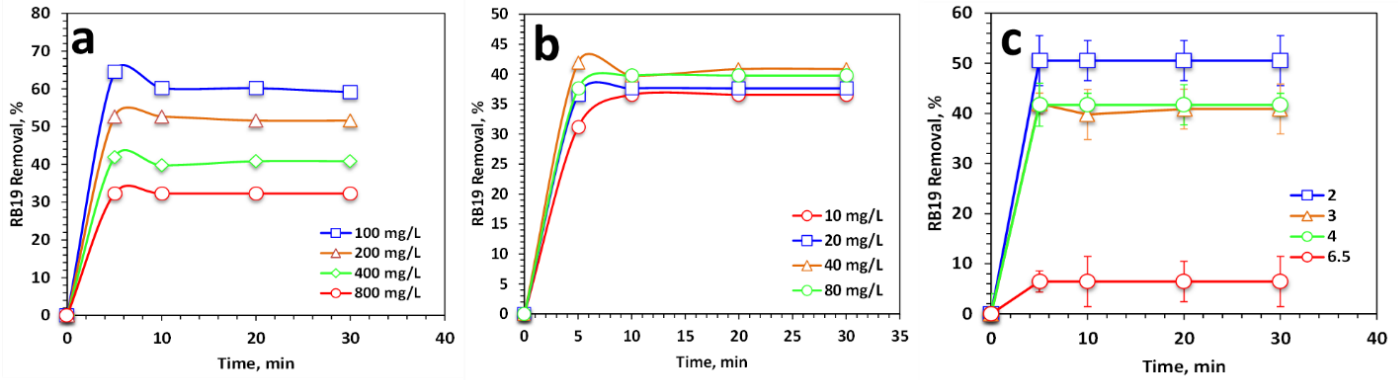

Figure 7. Influence of operational variables on RB19 oxidation. (**a**) Influence of H_2O_2, (**b**) influence of SCB:M dose, and (**c**) influence of pH.

Figure 7b demonstrates the operational dye removal and oxidation system by altering the doses within the 10–80 mg/L range. The treatment efficacy increased from 31% to 42% when the composite fiber catalyst dose was increased from 10 to 40 mg/L. However, elevating the extra magnetized SCB material to 80 mg/L lessens the oxidation effectiveness to only 37%. Photoactive hydroxo complex was generated and interacted with UV light photons to produce ·OH species. Metal ions in SCB and magnetite were created and attacked H_2O_2 to produce extra ·OH species. ·OH attacked RB19 particles to hydroxylate their aromatic rings to produce hydroxycyclohexadienyl radicals [21]. The same trend was observed previously by Thabet et al. [22]. Furthermore, it is important to note that the occurrence of dye desorption phenomena after reaching adsorption equilibrium time can negatively affect the dye removal rate over time [23,24]. However, this negative effect possessed a minor outcome (Figure 5a).

As the literature states, the iron/hydrogen peroxide reaction (Fenton oxidation) is sensitive to the medium pH [6,25]. Figure 7c represents that the decline in the pH value is related to an improvement in the RB19 concentration oxidation. This phenomenon confirms the Fenton reaction, which works in an active manner in an acidic pH medium. However, elevating the pH into the alkaline range resulted in reduced oxidation. This decline in the oxidation rate could be associated with H_2O_2 decomposition into water and oxygen [26].

Furthermore, this phenomenon is linked to pHpzc (the point of zero charge). Generally, the SCB surface is located near the neutral value [27]. Applying the solid addition method estimates it to be 6.7. As a result, the surface of SCB is positively charged. The high oxidation rate is observed at a strongly acidic pH mainly because of excess H^+ ions, and the RB19 molecules are easily adsorbed. This is because the electrostatic attraction forces of SCB and RB19 are positively and negatively charged, respectively [27]. Previous studies also reported similar results when treating cationic dye with bagasse materials [17]. Thus, pH is kept in the acidic range for further experiments.

2.7. Box/Behnken Model Design and Optimization

BBD of experiments (Tables 1 and 2) was applied to optimize the influencing parameters of the oxidation system.

Table 1. Box/Behnken design for independent parameters and their coded and un-coded boundaries applied.

Experimental Parameter	Representation		Codified Levels		
			Minimum	Medium	Maximum
	Un-Coded	Coded	−1	0	1
H_2O_2 (mg/L)	E_1	ε_1	50	100	150
SCB: M Catalyst (mg/L)	E_2	ε_2	30	40	50
pH	E_3	ε_3	2.0	2.5	3.0

Table 2. BBD cases of the RB19 oxidation technique for the 3 experimental parameters in codified and its related un-codified levels.

Case No.	Coded Values			Un-Coded Values			Response (%, Removal)	
	ε_1	ε_2	ε_3	E_1	E_2	E_3	Experimental	Predicted
1	−1	−1	0	50	40	2.5	80.05	73.88
2	−1	1	0	50	40	2.5	81.48	72.59
3	1	−1	0	150	40	2.5	50.92	59.80
4	1	1	0	150	40	2.5	45.37	51.53
5	0	−1	−1	100	30	2.0	56.07	48.87
6	0	−1	1	100	30	3.0	42.06	46.53
7	0	1	−1	100	50	2.0	41.48	37.18
8	0	1	1	100	50	3.0	41.66	48.67
9	−1	0	−1	50	30	2.0	43.33	46.21
10	1	0	−1	150	30	2.0	36.29	24.12
11	−1	0	1	50	40	3.0	34.11	46.27
12	1	0	1	150	40	3.0	36.11	33.22
13	0	0	0	100	40	2.5	86.21	86.19
14	0	0	0	100	40	2.5	86.23	86.19
15	0	0	0	100	40	2.5	86.15	86.19

The suggested polynomial quadratic equation confirms the related response of RB19 dye color removal ($\%y$) as follows:

$$y(\%) = 86.19 - 8.78E_1 - 2.38E_2 - 2.90E_3 - 14.79E_1^2 + 1.74E_1E_2 - 2.26E_1E_3 - 6.94E_2^2 + 3.54E_2E_3 - 33.93E_3^2 \quad (1)$$

To verify the statistical implication and the fitness of the suggested model, the F-test (Fisher's statistical) for ANOVA was tested and the data are exhibited in Table 3.

Table 3. Analysis of variance (ANOVA) for the regression model and the respective model terms.

Source	DF *	SS *	MS *	F-Value *	*p*-Value *
Model (Y)					
Regression	9	10.58333	1.175926	7.839506	0.017729
Linear	3	730.51292	730.512920	7.767593	1.003254
Quadratic	3	841.32800	841.328000	8.945898	1.426933
Cross Product	3	4480.80562	4480.805620	47.644713	0.725736
Error	5	470.23120	94.046240		
Total	14	6132.77700			
R^2	93.00%				
Adj-R^2	89.00%				

* DF: degree of freedom; SS: sum of squares; MS: mean squares; F-value: Fisher test; P: probability; R^2: coefficient of correlation; Adj-R^2 adjusted R^2.

Commonly, the fitness of the design is signified when the minimal standard deviation and a minimum probability value ($p < 0.005$) are recorded with a maximal factor of the regression coefficient (R^2) [28]. The model is accepted when the regression coefficient (R^2) value is not less than 80%.

The results displayed in Table 3 showed the high value of the R^2 regression coefficient (93%) with a minimal probability (p) value. Furthermore, the correlation between the predicted and experimental results was explored and the data attained showed a suitable correlation between the two models, as seen in Figure 8d.

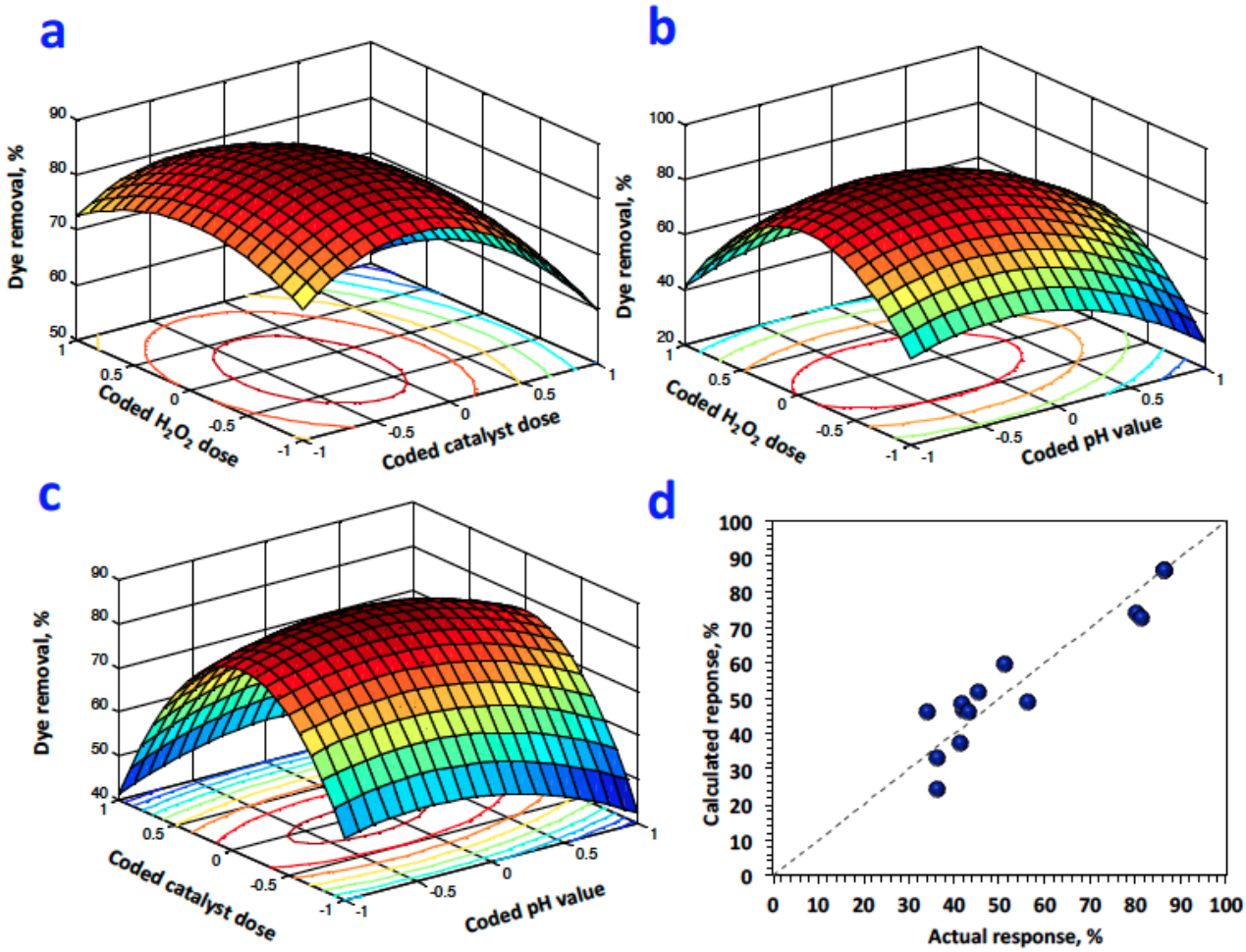

Figure 8. Box/Behnken (BBD) design system: (**a**) the 3D and 2D plot of y and the interacting influence of H_2O_2 and SCB:M; (**b**) the 3D and 2D plot of y and the interacting influence of H_2O_2 and pH; (**c**) the 3D and 2D plot of y and the interacting influence of SCB:M and pH; (**d**) the comparison of the original and estimated y of RB19 oxidation plot via BBD values.

The graphical presentation of the experimental variable's effects on the tested response is displayed in Figure 8a–c. The illustration represents the response data, indicating the main interactions with the proposed parameters. The surface (3D) graph and contour (2D) dimensional plots displayed in Figure 8a show the relationship between the RB19 color removal tendency of oxidation increase with the increase in both the doses of H_2O_2 and SCB:M reagents. But the curvature of the 3D surface (Figure 8a) reveals the interaction effect between the SCB:M and H_2O_2 doses. Such interactions are responsible for forming the highly OH-sensitive reaction intermediate species. Hydroxyl radicals are the main support of the RB19 oxidation reaction. An increase in such reagents means a declining RB19 oxidative rate. Therefore, the optimal ratio of SCB:M/H_2O_2 is required to exploit the hydroxyl radicals, which are the system's main oxidative radicals.

Additionally, a graphical illustration of the optimization exhibited in Figure 8b positions the area, which is the darker portion in the graph, for the optimal condition of the SCB:M /H_2O_2 system for RB19 removal. All the suggested parameters and their responses to the specific maximum and minimum limits of the predicted model region are suggestive and appropriate to the standard. Also, Figure 8c illustrates the relationship between the SCB:M reagent and the pH value. The suggested 3D and 2D plots indicate that the increased dose of the catalyst is increasing the oxidation of the dye. However, a low pH value results in an increased response. The curvature suggests the limits of expanding the dye's oxidation with the variables.

To further evaluate the suitability of the suggested design, Mathematica software achieved the predicted optimization of the operational values of the operating variables. The values are 85 and 39 mg/L for the peroxide and SCB-based material, respectively, at an optimal pH level of 2.5, while the predicted RB19 removal response is 92%. Hence, the proposed optimum values validate the model by conducting three additional test replicates. The measured response recorded a RB19 removal of 92.5%. This verifies that the RSM based on the BBD factorial model is acceptable for optimizing the operational parameters and prompting RB19 mineralization via the MSCB CRD-based oxidative nanoparticle composite system. Under the predicted optimum operating conditions, the chemical oxygen demand (COD) and total organic carbon (TOC) recorded a decrease of approximately 63% and 88%, respectively, which proves the effectiveness of the applied treatment.

2.8. Comparison of Various Sugarcane Bagasse-Based Treatment Systems

Table 4 compares the sugarcane bagasse/magnetite augmented catalytic photo-oxidative using the magnetized modified Fenton-type reaction (SCB:M/H_2O_2/UV) in the present investigation with other previously cited research work dealing with SCB. It can be determined from the data illustrated in Table 4 that the SCB:M /H_2O_2/UV oxidation applied in this study effectively treated the polluted water with anion RB19 dye, recording 92.5% removal. Thus, the system is comparable to other treatments which reached more than 90% (Table 4). However, such technologies result in secondary wastes that require further treatment, as they mainly depend on the adsorption process. On the other hand, the current environmentally benign system easily recovers due to the augmentation of magnetite nanoparticles with SCB. Moreover, applying the minimum reaction time and tiny amounts of the magnetite catalyst compared to other treatment processes, it is economically feasible. Also, it should be mentioned that adsorption transforms the pollutants' phase rather than mineralizing them upon applying Fenton's oxidation. This makes other treatments expensive since the formation of toxic end-products and sludge materials has been overcome in the current system since the pollutants are mineralized.

Table 4. Assessment of various cellulose-based treatment methodologies for various polluted effluents.

Treatment System	Aqueous Stream Pollutant	Operating Conditions				Removal %	Ref.
		Catalyst	pH	Temp. °C	Time min		
Oxid./Ads.	Reactive blue 19 dye	SCB:M (3:1) (39 mg/L)	2.5	30 °C	5	92.5	This work
Ads.	Methylene blue	TSCB	7	25 °C	30	96	[29]
Ads.	Basic Crystal violet dye	TSCB	7	25 °C	30	96	[29]
Ads.	Methylene blue	ISCB	8.4	25 °C	360	94	[30]
Ads.	Cadmium	(CNF)-ISCB	5	30 °C	70	99	[31]
Ads.	Pb(II)	(SBFB)	5	25 °C	120	99	[32]

SCB:M: sugarcane bagasse: Magnetite; TSCB: treated sugarcane bagasse; CNF: cellulose nanofibers; ISCB: iron-impregnated sugarcane bagasse; SBFB: sugarcane bagasse powder-doped iron (III) oxide-hydroxide beads; Ads.: adsorption.

2.9. Temperature Influence on Kinetic Parameters and Thermodynamic Behavior

Temperature plays a crucial role in oxidation-based reaction technology. Such significance is related to its effectiveness in terms of reaction rates and kinetics. In this regard, to assess the temperature influence on the proposed SCB:M sustainable-based oxidative system, tests were conducted over the range of 30–60 °C and the data presented in Figure 9a illustrate the reduction in RB19 dye removal efficacy from 44% to 3% for color removal with a temperature rise. This could be because H_2O_2 decomposes into O_2 and H_2O at elevated temperatures instead of forming reactive OH radicals. Hence, hydrogen peroxide is converted to a hydroxyl-active free radical scavenger instead of a generator. Consequently, the overall reaction rate is reduced. Additionally, the desorption step enhancement onto the SCB sorption procedure asserts the technology is exothermic [33]. Further, the temperature elevation weakens the active adsorption forces between the vacant positions on the SCB surface and the RB19 molecules, and likewise between the closest RB19 molecules on the adsorption site. Citations from earlier research showed a similar oxidation trend when using the adsorption technique to treat wastewater that was high in phenolics [34].

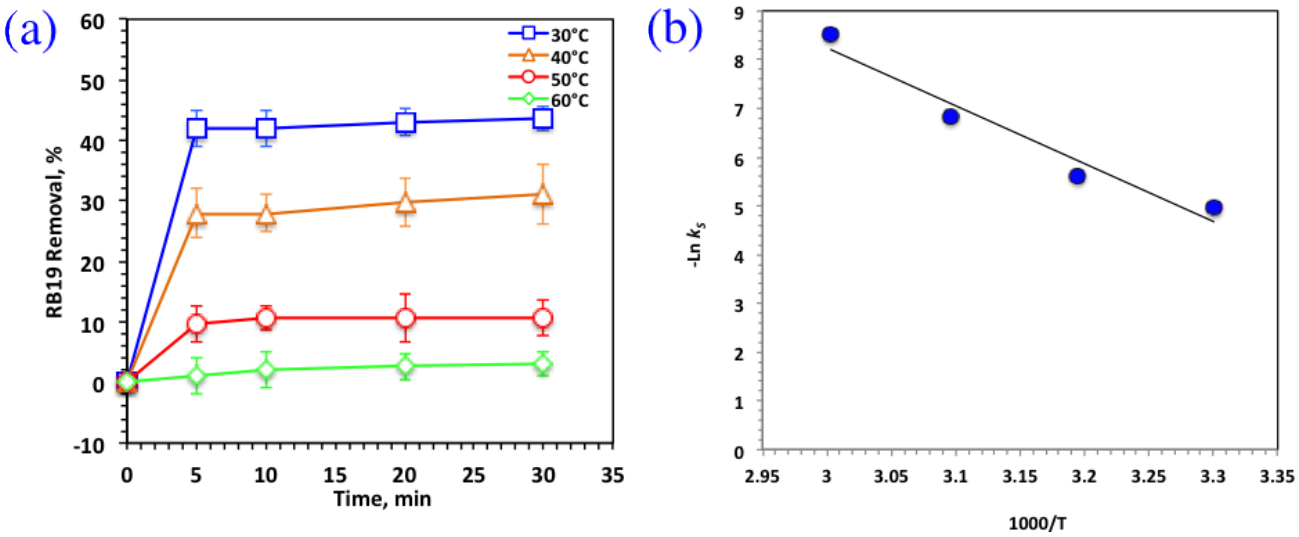

Figure 9. Thermal effect on the RB19 oxidation via SCB:M/H_2O_2 system. (**a**) Temperature effect; (**b**) the plot of ln k_S versus 1000/T (solid lines signify least-squares fitting).

Temperature's impact on the RB19 dye oxidation reaction has been additionally examined through kinetic and thermodynamic parameters. To acquire assessment for both reactor design and system control, which emphasizes the economics of the combined system process via capital and operating expenses [35], kinetic values were studied by using the linear type of zero-, first- and second-kinetic-order rate designs, and such estimated models are exhibited in Table 5. The adequacy of the displayed models was checked through their regression coefficient (r^2) values, where the maximum values were equivalent to the suitable model applied. According to the results in Table 4, the highest regression coefficient numbers matched the second-order kinetic model that proved the best fit of the data for RB19 elimination by the adapted SCB:M oxidation system. As presented in Table 5, the second-order model rate constants (k_S) are diminished from 0.069 to 0.0002 L mg^{-1} min^{-1} at 30 to 60 °C, respectively. Additionally, the equivalent half-life reaction time ($t_{0.5}$) declines with the temperature degree elevation. Such examination agrees with that formerly cited in the published research articles [36], as they proved the highest Fenton oxidation removal was attained at temperatures ranging from 17 to 38 °C under their experimental conditions.

Table 5. Statistical analysis of different kinetic models for RB19 oxidation via SCB:M (1:3) magnetized SCB/H_2O_2 *.

Kinetic Model	Linearized Eq.	Parameters	Values			
			T, °C			
			30 °C	40 °C	50 °C	60 °C
Zero-order	$C_t = C_o - k_Z t$	K_Z (min^{-1})	0.1805	0.1257	0.046	0.0134
		$t_{0.5}$	28.85	41.42	113.22	388.65
		r^2	0.49	0.52	0.53	0.88
First-order	$C_t = C_o - e^{k_F t}$	K_F (min^{-1})	0.0227	0.0154	0.0047	0.0013
		$t_{0.5}$ (min)	30.53	48.13	147.45	533.08
		r^2	0.55	0.62	0.58	0.96
Second-order	$\left(\frac{1}{C_t}\right) = \left(\frac{1}{C_0}\right) - k_S t$	K_S (L mg^{-1} min^{-1})	0.0069	0.0037	0.0011	0.0002
		$t_{0.5}$ (min)	13.91	25.95	87.28	480.03
		r^2	0.8	0.8	0.82	0.99

* C_o and C_t: initial and at time t dye concentration (mg L^{-1}); t: time (min); k_Z, k_F, and k_S: kinetic rate constants of zero-, first-, and second-order kinetic models, respectively.

To adequately explore the temperature's impact on the RB19 dye removal, the thermodynamic activation variables were attained through the Arrhenius fit, established based on the second-order kinetic model as given in Equation (2).

$$\ln k_S = \ln A - \frac{E_a}{RT} \quad (2)$$

where A is the pre-exponential factor constant; E_a is the energy of activation (kJ mol^{-1}); R is the gas constant (8.314 J mol^{-1} K^{-1}), and T is the temperature (K). The linearized relation between ln k_s versus 1/T is attained and plotted in Figure 9b. The plot displays a relation in which its slope is equivalent to ($-E_a/R$) that is applied to investigate E_a. The thermodynamic activation parameter of the RB19 removal was assessed by the Eyring Equation (3).

$$k_S = \frac{k_B T}{h} e^{\left(-\frac{\Delta G^\circ}{RT}\right)} \quad (3)$$

where k_B and h are Boltzmann and Planck's constants, respectively. Hence, the enthalpy (ΔH°) and the entropy (ΔS°) of activation might be examined from: $\Delta H^\circ = E_a - RT$ and $\Delta S^\circ = \left(\Delta H^\circ - \Delta G^\circ\right)/T$, respectively [37].

Table 6 represents the data attained from such relations and explores the non-spontaneous nature of the oxidative RB19 procedure because the (ΔG°) values were greater than 0 [23], and the extent of non-spontaneity increased when the temperature was elevated. The positive ΔH° values indicated and confirmed exothermic oxidation [24]. Additionally, the low and negative ΔS° data results verified the non-spontaneous class of the reaction system that exposed a decline in the degree of freedom of the RB19 spices and sustained a great hydroxyl species yield. Previously, Pourali et al. [38] cited the non-spontaneous nature of the oxidation reaction upon using a ZnO photocatalyst for oxidizing dye containing aqueous effluent. Additionally, the reaction proceeded at an energy barrier of approximately 98.66 kJ mol^{-1}. A similar observation was stated previously by Sun et al. [39] in treating phenolic compounds through the oxidative technique.

Table 6. Thermodynamics variables of RB19 oxidation via SCB:M (3:1) magnetized SCB/H_2O_2.

Thermodynamics Variables	T, °C			
	30 °C	**40 °C**	**50 °C**	**60 °C**
Ea (kJmol^{-1})		98.66		
ΔG° (kJmol^{-1})	86.78	91.35	97.61	105.44
ΔH° (kJmol^{-1})	96.14	96.05	95.97	95.89
ΔS° (Jmol^{-1}K^{-1})	30.88	15.03	−5.07	−28.67

2.10. Recyclability

The magnetized SCB catalyst's ability to be used again and again and to be stable enough to be recycled was a huge deal for its long-term use in this category of applications. Therefore, after use, the SCB:M catalyst was subjected to separation to be recovered for successive use after distilled water washing and oven-drying at 105 °C [22,40–42]. As illustrated in Figure 10, the catalyst showed good sustainability through a well-catalytic activity achieved through six cycles of reuse, with only a 7% reduction in its removal efficiency compared to the fresh one. Such catalysts' magnetic properties are considered superior because of their long-term catalyst recyclability for successive use. Hence, their removal from the final effluent after treatment is an easy option via an external magnet. Consequently, such investigation confirmed SCB:M's promise of sustainability in introducing them for industrial real wastewater treatment applications.

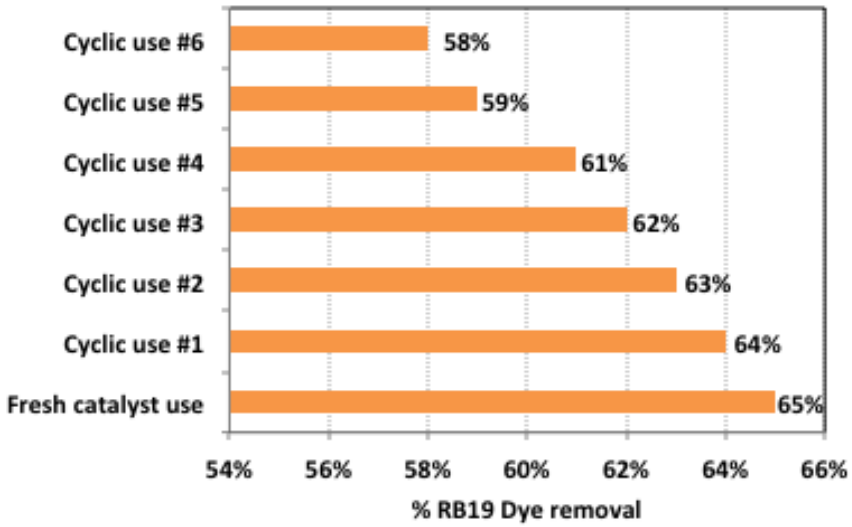

Figure 10. Influence of using SCB:M system in consecutive cycles.

3. Materials and Methods

3.1. Materials

Sugarcane bagasse material was taken from the Egyptian Petroleum Research Institute, as a spent waste from a bioethanol production process. Choline hydroxide and glycine were purchased from Sigma Aldrich (Taufkirchen, Germany). Ferrous and ferric sulfate (delivered by Qualikems Chemicals, Gujarat, India) were used as the precursors to prepare magnetite nanoparticles. H_2O_2 (40%, *w*/*w*) was added to initiate the oxidation system. The pH was adjusted using diluted H_2SO_4 and NaOH. All the chemicals were used as delivered, without extra purification.

3.2. Synthesis of Cholinium/Glycinate Ionic Liquid [Ch][Gly]

The preparation of [Ch][Gly] **3** ionic liquid (Scheme 1) was successfully performed via the reported method in the literature [16]. Choline hydroxide **1** (Scheme 1, 45% wt/wt, 50 mL, 1 mmol) was added to the glycine (**2** Scheme 1**,** 1 mmol) with stirring at 25 °C for

24 h followed by the removal of water using a rotatory evaporator for 3 h to achieve [Ch][Gly] in good yield (48%) and it showed data consistency with the prepared ionic liquid (c.f. Supplementary Materials).

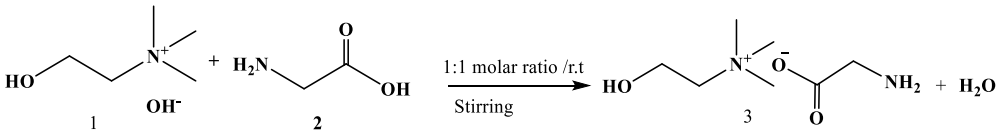

Scheme 1. Synthesis of cholinium/glycinate ionic liquid [Ch][Gly] **3**.

3.3. Synthesis of Nanocomposite

Initially, the collected SCB was washed several times with distilled water (DW) and dried overnight at 105 °C. In such a technique, 1.25 g of SCB was subjected to 25 g of [Ch][Gly] at 130 °C for 3 h. Afterward, the mixture was poured into 20 mL of acetone/ethanol (1:1 v/v) and stirred for 1h, followed by centrifugation of the mixture to obtain cellulose. The isolated cellulose was filtered and rinsed with DW. The acquired material was crushed to obtain a fine powder through subjection into milling by a ball mill machine (300 rpm for 10 h each h).

The environmentally benign co-precipitation route was used to synthesize the magnetite using ferrous (2M) and ferric sulfate (1M), a hybrid addition of their specific amounts with DW. Furthermore, NaOH solution was added in drops until the pH was recorded at 11. Then, the precipitate was attained in the solution, and the mixture was subsequently exposed to constant mixing (at 80 °C). Later, the as-prepared nanoparticles were repeatedly washed using DW until the neutral pH was reached to remove any remaining Na_2SO_4 and NaOH in the solution. Then, the attained solution was left for settling before filtration and washed with DW before oven-drying (60 °C) [41].

The produced Fe_3O_4 nanoparticles were ground with the extracted SCB in various mass ratio proportions of SCB:M (0:1, 1:1, 1:2, 1:0, 2:1, 3:1, and 5:1). The obtained solid mixture samples were preserved in a Petri dish and wetted with a few drops of DW before being subjected to a household microwave oven for 5 min at a power of 200 watts according to the procedure described elsewhere [9]. The SCB:M nanocomposites that were obtained look uniform brownish.

3.4. Photocatalytic Oxidation Set-Up

A stock solution of anionic dye, Reactive blue 19 aqueous solution, was prepared, and a dilution was carried out to attain the essential concentrations (5 to 30 ppm). A total of 100 mL of RB19 aliquot samples was poured into a 250 mL glass beaker. Initially, the pH of the aqueous mixture was adjusted, when needed, prior to the reagent's addition. The aqueous mixture and the reagent were subjected to ultrasonic diffusion before mechanical stirring, and ultraviolet radiation occurred in the photocatalytic reaction. A UV 254 nm lamp (15 W, 230 V/50 Hz) was used for irradiation, and all the tests were conducted at 25 ± 1 °C. Consequently, after definite periods, the samples were exposed for spectrophotometric analysis. All the analysis was performed in three replicates, and the average was recorded. Then, the recorded data, even in tables or figures, are the average values of at least three analyses.

3.5. Data Analysis and Analytical Procedures

The analysis of the dye in the wastewater substrate was monitored through the spectrophotometric method, which was applied at the highest absorbance wavelength peak (590 nm) of Reactive blue 19 via a UV–visible spectrophotometer (model Unico 2100-UV-Vis series spectrophotometer, Unico, Loveland, CO, USA).

The percentage of RB19 removal from the aqueous effluent was calculated according to Equation (4). The effluent's pH was monitored to a certain value, as essential, by a digital-type pH meter (model AD1030—Adwa, Szeged, Hungary).

$$\boldsymbol{y}(\%) = \frac{\boldsymbol{C_o} - \boldsymbol{C_t}}{\boldsymbol{C_o}} \times 100 \quad (4)$$

where C_o and C_t are the preliminary and final remaining RB19 doses in the polluted water solution, respectively.

3.6. Statistical Design for Modeling the Multiple Operating Parameters Effect

A response surface based on statistical methodological analysis (RSM) is signified as a significant model design system that is applied to improve the implementation of multivariable systems by signifying the relative consequence of multivariable parameters with the lowest conducted experiments in comparison to a complete factorial design matrix at an equal level. The chief role of RSM modeling is to offer a correlation between the controllable variables and the significant response. Box/Behnken design (BBD), based on the statistical RSM technique, is presented as a mathematical tool for optimizing the experimental operating parameter values [15,41]. BBD is chosen as a nonlinear multivariable design for response surface optimization that affects the various variables. Moreover, it can classify the relationship between the controlled parameters and the achieved response.

Through this study, RSM based on the BBD model was performed via Statistical Analysis Software (SAS 9.3, SAS Institute, Cary, NC, USA) to calculate the model of the RB19 removal (at the initial concentration of 10 mg/L) by regression analysis and ANOVA test (analysis of variance). The highest effective parameters in the photocatalytic system were selected to estimate their effect on Reactive blue 19 (RB19) removal, i.e., H_2O_2, SCB:M catalyst concentrations, and pH, to investigate their effect on RB19 load oxidation (γ) efficacy for removal from an aqueous stream. Three levels were selected for each of the three parameters: H_2O_2 (ε_1), SCB:M catalyst (ε_2), and pH (ε_3) as listed in Table 1 in the natural and coded numbers. The levels for each variable were determined according to preliminary experimental work.

Generally, the optimization performance includes principal steps and the statistical design experimental matrix (Table 2). Then, the approximation of the factors in the suggested mathematical design 16 and at the end predicting the response assesses the sufficiency of the proposed design. The model is well fitting by the polynomial second-order equation model (Equation (5)) in order to relate the correlative parameters.

$$\gamma = \beta_o + \sum \beta_i E_i + \sum \beta_{ii} E_i^2 + \sum \beta_{ij} E_i E_j \quad (5)$$

where γ is the RB19 oxidation response; βo, βi, βii, and βij are the model coefficient of the linear effect and double interactions; $\boldsymbol{E_i}$ and $\boldsymbol{E_i^2}$ are the independent variables.

The determination coefficient, R^2, was used to judge the attained polynomial equation significance. Moreover, the graphical representation was applied to visualize the influence of the independent system parameters and the response through three-dimensional (3D) surface and their particular two-dimensional (2D) contour plots. To locate the model design optimal required values, Mathematica software version V 5.2 was applied. The COD and TOC under the predicted optimum operating conditions have been measured in accordance with Nassar et al. [23] to evaluate the effectiveness of the applied treatment in the complete mineralization of the pollutant.

3.7. Characterization

The composition, microstructure, and morphology of the synthesized magnetite, SCB, and SCB:M samples were characterized. The structure of the arranged material composite was analyzed by X-ray diffractometry (XRD, X'pert, MPD3040, Phillips, Eindhoven,

The Netherlands) with *Cu-Kα* radiation at ambient conditions (λ = 1.5406 Å). That investigation used step-scan mode with intensities over the 2θ range of 5–80°.

Moreover, the morphologies of the prepared magnetite, SCB, as well as SCB:M samples, as abovementioned in Section 2.2, were examined and pictured through SEM (Field-emission scanning electron microscope with a model Quanta FEG 250, FEI Company, Eindhoven, the Netherlands) with different magnifications (×8000 and ×60,000). That was supplemented by energy-dispersive X-ray spectroscopy (EDS). The main metal oxides in SCB and SCB:M (3:1) were examined through the energy dispersive spectrum. Moreover, the magnetic characteristics were highlighted and investigated by measuring the vibration sample magnetometer (VSM, Lake Shore Cryotronics, Model 7410, Westerville, OH, USA) at room temperature.

4. Conclusions

The current work confirmed a feasible way to fabricate a sustainable cradle-to-cradle photocatalyst of sugarcane bagasse fiber-augmented magnetite nanoparticles via the microwave technique. The experimental results revealed that magnetized sugarcane bagasse could be a suitable alternate photocatalyst for RB19 elimination. The process was optimized for maximal dye removal and the optimized operating variables were 85 and 39 mg/L for H_2O_2 and SCB:M, respectively, at optimal pH 2.5 within 5 min of irradiance time. Also, the kinetic modeling was investigated and the data revealed that the reaction is well fitted with the second-order model kinetics. The results with kinetic constants ranged from 0.069 to 0.0002 L mg^{-1} min^{-1}. Furthermore, the reaction is signified as an exothermic reaction since the temperature elevation from room temperature to 60 °C decreased the dye removal rate to only 3%. The reaction progress is recorded at an energy barrier of 98.66 kJ mol^{-1}. The results from the current work confirmed the sustainability of waste SCB as a recyclable magnetized photocatalyst in eliminating textile effluent wastewater. The findings from this kind of work using synthetic textile dyeing effluent are thought to add to what is known about real-life textile facilities. Further research on the initiative fabrication of composite fibers with targeted properties is underway to expand their real-world applications.

Supplementary Materials: The following supporting information can be downloaded at: https://www.mdpi.com/article/10.3390/catal14060354/s1, NMR and FTIR spectra for the prepared ionic liquid [Ch][Gly] were presented in the supporting information file.

Author Contributions: Conceptualization, M.A.T., J.X., X.L. and I.E.T.E.-S.; methodology, M.A.T. and A.A.S.A.; software, M.H.; validation, M.A.T.; formal analysis, M.A.T.; investigation, M.A.T., N.S.E.-G., J.X., X.L. and I.E.T.E.-S.; resources, M.A.T.; data curation, M.A.T. and N.S.E.-G.; writing—original draft preparation, M.A.T., A.A.S.A. and I.E.T.E.-S.; writing—review and editing, M.A.T., N.S.E.-G., J.X., X.L. and I.E.T.E.-S.; supervision, M.A.T., N.S.E.-G., J.X., X.L. and I.E.T.E.-S.; project administration, M.H.; funding acquisition, M.H. All authors have read and agreed to the published version of the manuscript.

Funding: This paper is based upon work supported by the Egyptian Science, Technology, and Innovation Funding Authority (STDF) under grant number 43140. This work also was financially funded by the National Key R&D Program of China (Nos. 2021YFE0190800), National Natural Science Foundation of China (Nos. 22178343, 22238011), International Partnership Program of Chinese Academy of Sciences (No. 2023VMA0001), and Key R&D projects in Hunan Province (No. 2021SK2047). This research was also funded by the Deanship of Scientific Research at King Khalid University, grant number RGP2/36/44.

Data Availability Statement: All data used in this study are included in this manuscript.

Conflicts of Interest: The authors declare no conflicts of interest.

References

1. Mondal, M.I.H.; Haque, M.O.; Ahmed, F.; Pervez, M.N.; Naddeo, V.; Ahmed, M.B. Super-Adsorptive Biodegradable Hydrogel from Simply Treated Sugarcane Bagasse. *Gels* **2022**, *8*, 177. [CrossRef] [PubMed]
2. Emam, H.E.; Ahmed, H.B.; Bechtold, T. In-situ deposition of Cu_2O micro-needles for biologically active textiles and their release properties. *Carbohydr. Polym.* **2017**, *165*, 255–265. [CrossRef] [PubMed]
3. Mahmud, M.A.; Anannya, F.R. Sugarcane bagasse—A source of cellulosic fiber for diverse applications. *Heliyon* **2021**, *7*, e07771. [CrossRef] [PubMed]
4. Saravanan, A.; Senthil Kumar, P.; Jeevanantham, S.; Karishma, S.; Tajsabreen, B.; Yaashikaa, P.R.; Reshma, B. Effective water/wastewater treatment methodologies for toxic pollutants removal: Processes and applications towards sustainable development. *Chemosphere* **2021**, *280*, 130595. [CrossRef] [PubMed]
5. Silva, J.A. Wastewater Treatment and Reuse for Sustainable Water Resources Management: A Systematic Literature Review. *Sustainability* **2023**, *15*, 10940. [CrossRef]
6. Rezgui, S.; Díez, A.M.; Monser, L.; Adhoum, N.; Pazos, M.; Sanromán, M.A. $ZnFe_2O_4$-chitosan magnetic beads for the removal of chlordimeform by photo-Fenton process under UVC irradiation. *J. Environ. Manag.* **2021**, *283*, 111987. [CrossRef] [PubMed]
7. Zhou, Y.; Zhang, L.; Cheng, Z. Removal of organic pollutants from aqueous solution using agricultural wastes: A review. *J. Mol. Liq.* **2015**, *212*, 739–762. [CrossRef]
8. Iwuozor, K.O.; Oyekunle, I.P.; Oladunjoye, I.O.; Ibitogbe, E.M.; Olorunfemi, T.S. A Review on the Mitigation of Heavy Metals from Aqueous Solution using Sugarcane Bagasse. *Sugar Tech* **2022**, *24*, 1167–1185. [CrossRef]
9. Ali, N.; El-Harbawi, M.; Abo Jabal, A.; Yin, C.-Y. Characteristics and oil sorption effectiveness of kapok fibre, sugarcane bagasse and rice husks: Oil removal suitability matrix. *Environ. Technol.* **2012**, *33*, 481–486. [CrossRef]
10. Tajernia, H.; Ebadi, T.; Nasernejad, B.; Ghafori, M. Arsenic Removal from Water by Sugarcane Bagasse: An Application of Response Surface Methodology (RSM). *Water Air Soil Pollut.* **2014**, *225*, 2028. [CrossRef]
11. Ullah, S.F.; Rong, A.; Nawshad, M. Editorial: Properties and Applications of Ionic Liquids in Energy and Environmental Science. *Front. Chem.* **2020**, *8*, 627213. [CrossRef] [PubMed]
12. Gadilohar, B.L.; Shankarling, G.S. Choline based ionic liquids and their applications in organic transformation. *J. Mol. Liq.* **2017**, *227*, 234–261. [CrossRef]
13. Tzani, A.; Karadendrou, M.-A.; Kalafateli, S.; Kakokefalou, V.; Detsi, A. Current Trends in Green Solvents: Biocompatible Ionic Liquids. *Crystals* **2022**, *12*, 1776. [CrossRef]
14. Gusrianto, P.; Zulharmita, H.R.; Rivai, H. Preparasi dan Karakterisasi Mikrokristalin Selulosa dari Limbah Serbuk Kayu Penggergajian. *J. Sains dan Teknol. Farmasi* **2011**, *16*, 180–188.
15. Ungureanu, N.; Vlăduț, V.; Biriș, S.-Ș. Sustainable Valorization of Waste and By-Products from Sugarcane Processing. *Sustainability* **2022**, *14*, 11089. [CrossRef]
16. Liu, Y.; Nie, Y.; Lu, X.; Zhang, X.; He, H.; Pan, F.; Zhou, L.; Liu, X.; Ji, X.; Zhang, S. Cascade utilization of lignocellulosic biomass to high—Value products. *Green Chem.* **2019**, *21*, 3499–3535. [CrossRef]
17. Tony, M.A. An industrial ecology approach: Green cellulose-based bio-adsorbent from sugar industry residue for treating textile industry wastewater effluent. *Int. J. Environ. Anal. Chem.* **2021**, *101*, 167–183. [CrossRef]
18. Unal, B.O.; Bilici, Z.; Ugur, N.; Isik, Z.; Harputlu, E.; Dizge, N.; Ocakoglu, K. Adsorption and Fenton oxidation of azo dyes by magnetite nanoparticles deposited on a glass substrate. *J. Water Process. Eng.* **2019**, *32*, 11.
19. Li, H.; Liu, L.; Cui, J.; Cui, J.; Wang, F.; Zhang, F. High-efficiency adsorption and regeneration of methylene blue and aniline onto activated carbon from waste edible fungus residue and its possible mechanism. *RSC Adv.* **2020**, *10*, 14262–14273. [CrossRef]
20. Ahmed, S.A.; Soliman, E.M. Silica coated magnetic particles using microwave synthesis for removal of dyes from natural water samples: Synthesis, characterization, equilibrium, isotherm and kinetics studies. *Appl. Surf. Sci.* **2013**, *284*, 23–32. [CrossRef]
21. Chen, R.; Pignatello, J.J. Role of quinone intermediates as electron shuttles in Fenton and photoassisted Fenton oxidations of aromatic compounds. *Environ. Sci. Technol.* **1997**, *31*, 2399–2406. [CrossRef]
22. Thabet, R.H.; Tony, M.A.; El Sherbiny, S.A.; Ali, I.A.; Fouad, M.K. Catalytic oxidation over nanostructured heterogeneous process as an effective tool for environmental remediation. *IOP Conf. Ser. Mater. Sci. Eng.* **2020**, *975*, 012004. [CrossRef]
23. Nassar, H.N.; El-azab, W.I.M.; El-Gendy, N.S. Sustainable ecofriendly recruitment of bioethanol fermentation lignocellulosic spent waste biomass for the safe reuse and discharge of petroleum production produced water via biosorption and solid biofuel production. *J. Hazard. Mater.* **2022**, *422*, 126845. [CrossRef] [PubMed]
24. El-Gendy, N.S.; Nassar, H.N. Study on the effectiveness of spent waste sugarcane bagasse for adsorption of different petroleum hydrocarbons water pollutants: Kinetic and equilibrium isotherm. *Desalin. Water Treat.* **2016**, *57*, 5514–5528. [CrossRef]
25. Shanmugam, B.K.; Easwaran, S.N.; Mohanakrishnan, A.S.; Kalyanaraman, C.; Mahadevan, S. Biodegradation of tannery dye effluent using Fenton's reagent and bacterial consortium: A biocalorimetric investigation. *J. Environ. Manag.* **2019**, *242*, 106–113. [CrossRef] [PubMed]
26. Maha, A.; Tony, M.M.E. End-of-life waste criteria: Synthesis and utilization of Mn-Zn ferrite nanoparticles as a super paramagnetic photocatalyst for synergistic wastewater remediation. *Appl. Water Sci.* **2021**, *12*, 21.
27. Fayoud, N.; Tahiri, S.; Younssi, S.A.; Albizane, A.; Gallart-Mateu, D.; Cervera, M.L.; De la Guardia, M. Kinetic, isotherm and thermodynamic studies of the adsorption of methylene blue dye onto agro-based cellulosic materials. *Desalin. Water Treat.* **2016**, *57*, 16611–16625. [CrossRef]

28. El-Geundi, M.S.; Nassar, M.M.; Farrag, T.E.; Ahmed, M.H. Methomyl adsorption onto Cotton Stalks Activated Carbon (CSAC): Equilibrium and process design. *Procedia Environ. Sci.* **2013**, *17*, 630–639. [CrossRef]
29. El Naeem, G.A.; Abd-Elhamid, A.I.; Farahat, O.O.; El-Bardan, A.A.; Soliman, H.M.; Nayl, A.A. Adsorption of crystal violet and methylene blue dyes using a cellulose-based adsorbent from sugercane bagasse: Characterization, kinetic and isotherm studies. *J. Mater. Res. Technol.* **2022**, *19*, 3241–3254.
30. Buthiyappan, A.; Jayaprina, G.; Abdul Aziz, A.R. Synthesis of iron oxides impregnated green adsorbent from sugarcane bagasse: Characterization and evaluation of adsorption efficiency. *J. Environ. Manag.* **2019**, *249*, 109323. [CrossRef] [PubMed]
31. Dehvari, M.; Behzad, J.; Sahand, J.; Sudabeh, P.; Zahra, S. Cadmium removal from aqueous solution using cellulose nanofibers obtained from waste sugarcane bagasse (SCB): Isotherm, kinetic, and thermodynamic studies. *Desalin. Water Treat.* **2021**, *221*, 218–228. [CrossRef]
32. Praipipat, P.; Pimploy, N.; Amornrat, S. Modification of sugarcane bagasse with iron (III) oxide-hydroxide to improve its adsorption property for removing lead (II) ions. *Sci. Rep.* **2023**, *13*, 1467. [CrossRef] [PubMed]
33. Zhang, Z.; Moghaddam, L.; O'Hara, I.M.; Doherty, W.O.S. Congo Red adsorption by ball-milled sugarcane bagasse. *Chem. Eng. J.* **2011**, *178*, 122–128. [CrossRef]
34. Parker, H.L.; Budarin, V.L.; Clark, J.H.; Hunt, A.J. Use of starbon for the adsorption and desorption of phenols. *ACS Sustain. Chem. Eng.* **2013**, *1*, 1311–1318. [CrossRef]
35. Al, M.F.; Moayyad, S.; Ahmad, S.; Mohammad, A.S. Impact of Fenton and ozone on oxidation of wastewater containing nitroaromatic compounds. *J. Environ. Sci.* **2008**, *20*, 675–682.
36. Pintor, A.M.A.; Vilar, V.J.P.; Boaventura, R.A.R. Decontamination of cork wastewaters by solar-photo-Fenton process using cork bleaching wastewater as H_2O_2 source. *Sol. Energy* **2011**, *85*, 579–587. [CrossRef]
37. Ahmadi, M.; Behin, J.; Mahnam, A.R. Kinetics and thermodynamics of peroxydisulfate oxidation of Reactive Yellow 84. *J. Saudi Chem. Soc.* **2016**, *20*, 644–650. [CrossRef]
38. Pourali, P.; Behzad, M.; Arfaeinia, H.; Ahmadfazeli, A.; Afshin, S.; Poureshgh, Y.; Rashtbari, Y. Removal of acid blue 113 from aqueous solutions using low-cost adsorbent: Adsorption isotherms, thermodynamics, kinetics and regeneration studies. *Sep. Sci. Technol.* **2021**, *56*, 3079–3091. [CrossRef]
39. Sun, J.H.; Sun, S.P.; Fan, M.H.; Guo, H.Q.; Qiao, L.P.; Sun, R.X. A kinetic study on the degradation of p-nitroaniline by Fenton oxidation process. *J. Hazard. Mater.* **2007**, *148*, 172–177. [CrossRef] [PubMed]
40. Tony, M.A.; Lin, L.-S. Iron Coated-Sand from Acid Mine Drainage Waste for Being a Catalytic Oxidant Towards Municipal Wastewater Remediation. *Int. J. Environ. Res.* **2021**, *15*, 191–201. [CrossRef]
41. Tony, M.A. Central composite design optimization of Bismarck Dye oxidation from textile effluent with Fenton's reagent. *Appl. Water Sci.* **2020**, *10*, 108. [CrossRef]
42. Pinheiro, D.R.; Neves, R.d.F.; Paz, S.P.A. A sequential Box-Behnken Design (BBD) and Response Surface Methodology (RSM) to optimize SAPO-34 synthesis from kaolin waste. *Microporous Mesoporous Mater.* **2021**, *323*, 111250. [CrossRef]